AIMS Mathematics, 9(3): 5905–5924.
DOI: 10.3934/math.2024288
Received: 24 November 2023
Revised: 06 January 2024
Accepted: 15 January 2024
Published: 31 January 2024

https://www.aimspress.com/journal/Math

Research article

Accelerating biomedical image segmentation using equilibrium optimization with a deep learning approach

Eman A. Al-Shahari[1], Marwa Obayya[2], Faiz Abdullah Alotaibi[3], Safa Alsafari[4], Ahmed S. Salama[5], and Mohammed Assiri[6,*]

[1] Department of Biology, College of Science & Arts at Mahayil, King Khalid University, Mohail Asser, Saudi Arabia
[2] Department of Biomedical Engineering, College of Engineering, Princess Nourah bint Abdulrahman University, P.O. Box 84428, Riyadh 11671, Saudi Arabia
[3] Department of Information Science, College of Humanities and Social Sciences, King Saud University, P. O Box 28095, Riyadh 11437, Saudi Arabia
[4] Department of Computer Science and Artificial Intelligence, College of Computer Science and Engineering, University of Jeddah, Jeddah 23890, Saudi Arabia
[5] Department of Electrical Engineering, Faculty of Engineering & Technology, Future University in Egypt, New Cairo 11845, Egypt
[6] Department of Computer Science, College of Sciences and Humanities- Aflaj, Prince Sattam bin Abdulaziz University, Aflaj 16273, Saudi Arabia

*** Correspondence: Email:** m.assiri@psau.edu.sa.

Abstract: Biomedical image segmentation is a vital task in the analysis of medical imaging, including the detection and delineation of pathological regions or anatomical structures within medical images. It has played a pivotal role in a variety of medical applications, involving diagnoses, monitoring of diseases, and treatment planning. Conventionally, clinicians or expert radiologists have manually conducted biomedical image segmentation, which is prone to human error, subjective, and time-consuming. With the advancement in computer vision and deep learning (DL) algorithms, automated and semi-automated segmentation techniques have attracted much research interest. DL approaches, particularly convolutional neural networks (CNN), have revolutionized biomedical image segmentation. With this motivation, we developed a novel equilibrium optimization algorithm with a deep learning-based biomedical image segmentation (EOADL-BIS) technique. The purpose of the EOADL-BIS technique is to integrate EOA with the Faster RCNN model for an accurate and efficient biomedical image segmentation process. To

accomplish this, the EOADL-BIS technique involves Faster R-CNN architecture with ResNeXt as a backbone network for image segmentation. The region proposal network (RPN) proficiently creates a collection of a set of region proposals, which are then fed into the ResNeXt for classification and precise localization. During the training process of the Faster RCNN algorithm, the EOA was utilized to optimize the hyperparameter of the ResNeXt model which increased the segmentation results and reduced the loss function. The experimental outcome of the EOADL-BIS algorithm was tested on distinct benchmark medical image databases. The experimental results stated the greater efficiency of the EOADL-BIS algorithm compared to other DL-based segmentation approaches.

Keywords: image processing; biomedical image segmentation; computer vision; deep learning; equilibrium optimizer
Mathematics Subject Classification: 11Y40

1. Introduction

The Medical Imaging technique plays a crucial role in the current medical system to perform non-invasive diagnostic processes, which includes the formation of functional and visual representations of the internal organs and human body for medical analysis [1]. It has various types comprised such as X-ray-based techniques, namely Computed Tomography (CT), traditional X-ray, mammography, ultrasound (US) imaging, molecular imaging method, and Magnetic Resonance Imaging (MRI). Other than these medical image methods, medical images can progressively be deployed to analyze different conditions, particularly those interrelated to the skin [2]. There exist 2 elements of medical images: One is image reconstruction and formation and the other is image processing and analysis [3]. Image formation includes a series of procedures whereby 2-D images of 3-D objects are designed. The reconstructions are dependent upon a group of iterative methods to construct 2-D and 3-D images usually in the object projection data. In contrast, image processing is used to improve image properties such as noise removal whereas image analysis extracts a group of features or quantitative information in the image for classification and detection of objects.

Medical image segmentation is the process of labeling all the pixels of the object from medical images [4]. Generally, it is an important task for healthcare applications and is different from Computer Aided Diagnoses (CADx) to lesion diagnosis for the planning and guiding of treatment. Medical image segmentation supports a physician's concentration for a specific region of the disease and extracts the data for highly correct diagnoses. The primary concerns related to medical image segmentation are the inaccessibility of huge annotated counts, lack of conventional segmentation protocol, low-quality images, a huge variation of images between the patients, and lack of high-quality labeled images for training [5]. This specifies the need for generalizable, automatic, and effective semantic image segmentation techniques [6]. The application of a Machine Learning (ML) based image segmentation method was used for classifying the ROI, viz., healthy area or diseased area.

On the other hand, the Deep Learning (DL) technique can able to process natural data in its raw procedure, so it no longer requires hand-crafted features [7]. These techniques are efficiently utilized for semantic segmentation on nature images and are created applications in biomedical image segmentation [8]. Extensive use of the DL technique can be assisted because rapid Graphic Processing Units (GPUs) and Central Processing Units (CPUs) can greatly decrease the training and implementation

time, access to vast amounts of data, and advances in learning methods [9]. Like traditional NN, Convolutional Neural Networks (CNNs) are extensively utilized among several DL architectures. CNN has demonstrated promising performance for automatic medical image segmentation. Furthermore, robustness, viz., the ability of the model to execute on complex images, and generalization viz., the ability of the model to carry out in an independent database are essential for the progress of Artificial Intelligence (AI) technology that is employed in medical tests [10]. Hence, there is a need for designing an effective architecture i.e., generalizable and robust across various biomedical applications.

We focused on the design of a novel equilibrium optimization algorithm with deep learning-based biomedical image segmentation (EOADL-BIS) technique. The EOADL-BIS technique performs segmentation process using involves Faster R-CNN model with ResNeXt as a backbone network. Besides, the EOA can be applied as a hyperparameter optimization approach of the ResNeXt model to boost the segmentation results and reduce the loss function. The performance validation of the EOADL-BIS technique takes place on various benchmark medical image databases and the results are inspected in terms of different measures.

2. Related works

In [11], the authors present 3 distinct multiscale dense connections (MDC) for encoding, the decoding of U_shaped structures, and across them. According to 3 dense connections, the authors present an MDC with U_Net (MDU_Net) for bio-medical image segmentation. MDU_Net straight fuses the adjacent mapping feature with various scales in either lower or higher layers for strengthening feature propagation in the present layer. In [12], the authors utilized the attention-based Transformer under the encoded and decoded phases for improving feature discrimination at the spatial level details and semantic place by its multi-head-based self-attention. Finally, the author's present structure named EG-TransUNet comprises 3 component elements enhanced by transformers semantic guidance attention, progressive enhancement, and channel spatial attention.

Tomar et al. [13] examined a new structure termed a feedback attention network (FANet), which unifies the preceding epoch mask with the mapping feature of the existing trained epoch. The preceding epoch mask is then utilized for providing hard attention to learn mapping features at distinct convolution layers. The authors [14] introduced a novel lightweight structure termed CNL-UNet for 2-D multi-modal bio-medical image segmentation. The presented CNL-UNet takes a pre-training encoded developed with TL approaches for learning suitably in fewer data counts. It takes adapted skip connections for reducing semantic gaps among the equivalent level of the encoded-decoded layer. Additionally, the presented structure was improved with a novel Classifier and Localizer (CNL) element.

Srivastava et al. [15] introduced a new structure termed a Multi-Scale Residual Fusion Network (MSRF-Net), which can be particularly planned for biomedical image segmentation. The presented MSRF-Net was capable of exchanging multi-scale features of distinct receptive domains employing a DSDF block. Zhao et al. [16] developed a deep active semi-supervised learning structure, the DSAL containing semi-supervised learning and active learning approaches. In DSAL, a novel condition dependent upon a deep supervision process is presented for selecting informative instances with lower and higher uncertainties for weak and strong labelers correspondingly.

Meng et al. [17] developed an easy, intuitive DL-based contour regression method. The authors establish a new multilevel, multistage aggregated network for regressing the control of the contour of samples directly in an endwise approach. The presented network seamlessly connects CNN with the

Attention Refinement module (AR) and GCN. Also, this method pays attention to object contours with the utilization of AR and GCN. Ibtehaz and Rahman [18] introduced a new structure, MultiResUNet, as the probable successor to the U-Net structure. The authors are tested and related to MultiResUNet with typical U-Net on the massive repertoire of multi-modal medical images.

Ma et al. [19] developed a great new building block, the hyper-convolution, which discreetly signifies the convolution kernel as a role of kernel synchronizes. Hyper-convolutions allow decoupling of the kernel size, and therefore its receptive area, from the number of learnable parameters. Song et al. [20] presented an Outlined Attention U-networks (OAU-nets) with a bypass branching plan to resolve biomedical image segmentation tasks, which is proficient in detecting deep and shallow features. In [21], we classified annotation noise in image segmentation tasks, presented techniques to pretend annotation noise, and inspected the effect on the segmentation excellence. Dual new automatic models to recognize intra-annotator and inter-annotator discrepancies dependent upon uncertainty-aware deep neural networks (DNNs) are projected. Mansour et al. [22] proposed a new AI-based fusion technique for CRC disease classification and diagnosis, called AIFM-CRC. Besides, a fusion-based feature removal procedure takes place where the Inception v4-based deep features and SIFT-based handcrafted features have been joined together. Also, the whale optimizer algorithm tuned deep support vector machine method is used as a classification model to define the reality of CRC.

3. The proposed model

In this study, we concentrated on the development and design of the EOADL-BIS technique for biomedical image segmentation. The main intention of the EOADL-BIS technique is to combine EOA with the Faster RCNN model for an accurate and efficient biomedical image segmentation process. The EOADL-BIS technique comprises two major phases of operations Faster RCNN-based image segmentation and EOA-based hyperparameter tuning. Figure 1 illustrates the workflow of the EOADL-BIS approach.

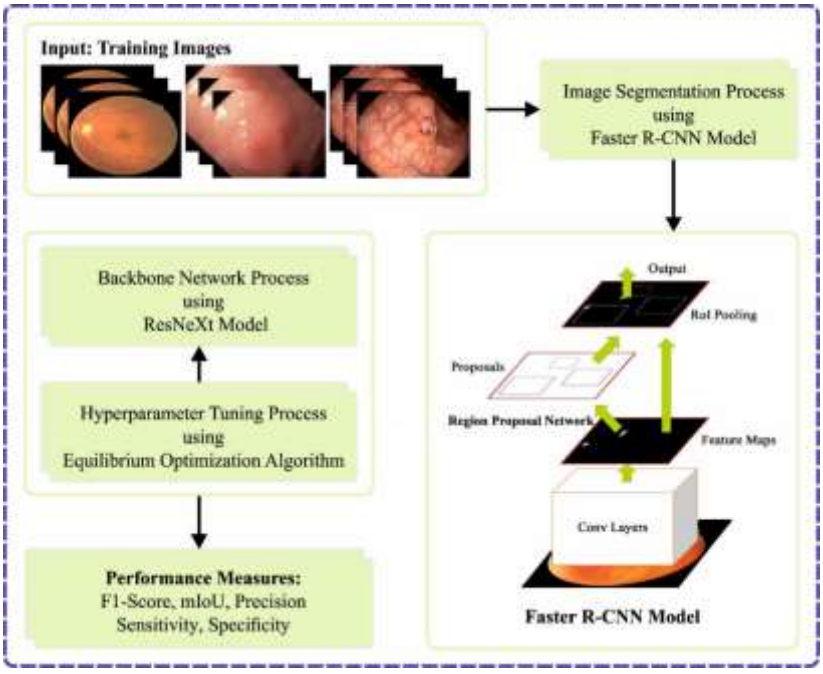

Figure 1. Workflow of EOADL-BIS algorithm.

3.1. Image segmentation using Faster RCNN

To segment the biomedical images, the Faster RCNN model is used. Fast RCNN combines region proposal network (RPN) and Fast RCNN. Fast RCNN consists of two modules namely, fast RCNN detector and RPN proposing regions. First, the entire images are inputted into ResNeXt for feature extraction. In this paper, the ResNeXt architecture adopted could stack deep network models to enhance the detection performance, but decrease the hyperparameter count [23].

It changes the concept of the classical ResNet and VGG networks stacking, borrows the Inception network sequences division transformation aggregation approach, and transmits the single path convolutional to various convolutions of different branches with a similar topology strategy, facilitating transplantation, and decreasing the design of hyperparameters. The ResNeXt exploits a Block infrastructure with grouped convolution. Here, an input feature matrix endures dimensionality decrease using 1×1 convolution kernels, which reduces the channel count to half of its original values. Then, 32 convolution groups can be exploited, every comprising 3×3 convolution sizes, for feature extraction purposes. Consequently, the extracted feature was concatenated and aggregated. Last, the inputs and outputs are added after the convolution kernel is size and, the last output can be attained by activating the ReLu function.

$$y = x + \sum_{i=1}^{C} T_i(x) \tag{1}$$

where y refers to the output; X denotes the input; Cshows the base number; and $T_i(x)$ indicates i^{th} point mapping functions.

Fast RCNN adapts RPN for candidate region generation, different Fast R-CNN utilizing the selective search method, and around 300 candidate region proposal was produced for every image [24]. Then, the region proposal was mapped to the mapping feature of the final convolution layer of VGG-16. The mapping feature is not of equal dimensions. Thus, the region proposal should be inputted to the RoI for processing. The features of the integrated size are eventually inputted to the FC layer for completing the task. Fast RCNN decreases the count of region proposals in the original 12000 to 300. It enhances the accuracy of detection and optimizes the quality of region proposals.

The core of Fast RCNN is RPN which considerably decreases the generated count of regional proposals. RPN is used to find a pixel via a sliding window on the mapping feature. Next, the pixel can be utilized as the center point for extracting 9 rectangular regions with 3 aspect ratios (1:3, 1:2, 1: 1) and three scales $(128^2,\ 256^2, 512^2)$, which are named anchors. It resolves the problems of multiscale objects. There are several pixels on the feature map and one pixel is equivalent to 9 anchors that create a considerable number of anchors. Each anchor could not participate in the training, for screening a specific number of instances. The region proposal can be produced by input images as to the RPN network for the forward computation to attain the frame regression parameter of anchor and classification probability.

The loss function can be evaluated using Eq (2):

$$L(\{p_i\},\{t_i\}) = \frac{1}{N_{cls}} \sum_i L_{cls}\,(p_i, p_i^*)$$

$$+\lambda \frac{1}{N_{reg}} \sum_i p_i^*\, L_{reg}(t_i, t_i^*) \tag{2}$$

In Eq (2), i denotes the index of the anchor. p_i indicates the probability of predicted anchor i. p_i^* shows the ground-truth label. t_i represents the vector representing 4 parameterized coordinates of the forecasted box, and t_i^* denotes the ground truth box. $L_{cls}(p_i, p_i^*)$ and $L_{reg}(t_i, t_i^*)$ characterize classification loss and regression loss, correspondingly.

$$L_{cls}(p_i, p_i^*) = -\log[p_i^* p_i + (1 - p_i^*)(1 - p_i)] \tag{3}$$

$$L_{reg}(t_i, t_i^*) = R(t_i - t_i^*) \tag{4}$$

where R indicates the smooth L1 function. The term $p_i^* L_{reg}$ implies the regression loss is activated only for positive anchor $(p_i^* = 1)$ and is restricted or else $(p_i^* = 0)$. $\{p_i\}$ and $\{t_i\}$ are outputs of regression and classification layers. The 2 terms can be normalized using N_{reg} and N_{cls} weighted by balancing parameter λ. N_{reg} can be normalized by the number of anchor positions. N_{cls} can be normalized by the minibatch size. By default, it can be fixed to $\lambda = 10$, and thereby the 2 terms can be weighted equally.

3.2. Hyperparameter Tuning using EOA

To adjust the hyperparameter values of the ResNeXt model, the EOA is employed. EOA is a physical law-based metaheuristic technique newly established [25]. Based on the volume control, EOA makes use of the dynamic mass balancing method. The mathematical model is used for expressing mass balance to specify the concentration of non-reactive elements in the dynamic control volume (CV) environments. This equation can be described as a function with several procedures in different sink and source conditions. The 1st-order differential equation represents the common mass balance formula. It describes the mass quantity that enters the method plus the amount generated minus the amount which proceeds the method as a time function.

$$V\frac{dC}{dt} = QC_{eq} - QC + G \tag{5}$$

In Eq (5), C shows the concentration of CV (V), Q indicates the volumetric flow rate (in and out of CV), $V\frac{dC}{dt}$ indicates the rate of mass change from the CV, QC_{eq} refers to concentration in the equilibrium state, $V\frac{dC}{dt}$ reaches zero for attaining the steady state equilibrium and G shows the rate of mass generation from the CV.

The resulting equation is used to determine the concentration from the CV (C) after reorganizing Eq (5) as a time function and integration is given below:

$$C = C_{eq} + \left(C_0 - C_{eq}\right) \times F + \frac{G}{\lambda \times V} \times (1 - F) \tag{6}$$

Eq (6) calculates the concentration of CV with the identified rate of turnover or evaluates the average rate of turnover through linear regression with the recognized rate of generation and other parameters. Furthermore, F is evaluated as follows:

$$F = exp[-\lambda \times (t - t)] \tag{7}$$

In Eq (7), t_0 and C_0 in the prior equation represent the starting time and concentration, correspondingly that is reliant on the integration interval.

The main framework of EOA is composed of several equations. The concentration is the same as the position of the particle, and the word particle represents a proposed solution. Three terms available in Eq (6) are:

- C_{eq} refers to the concentration of equilibrium, and it represents the most efficient options selected randomly in the pool of equilibrium.
- $(C_0 - C_{eq})$ represent the difference in variance amongst the equilibrium state C_{eq} and particle C_0. It is responsible to search the area for macro-searches.
- $\frac{G}{\lambda \times V}$ indicates the higher generation rate to hit notable exploitation that assists with exploration while staying away from a local minimum.

Based on this concept, the explanation of EOA is discussed below:

Within the specific search region, the arbitrary population (primary concentration) was initialized using the normal distribution based on the particle number and dimensional.

$$C_i^{initial} = C_{\min} + rand_i(C_{\max} - C_{\min}), i = 1,2,\dots,n \tag{8}$$

In Eq (8), n indicates the population size, $C_i^{initial}$ represents the initial concentration vector of i^{th} particles, $C_{\max}$ and $C_{\min}$ indicate the upper and lower bound, correspondingly, and $rand_i$ refers to the uniform random number generated within [0,1]. Figure 2 depicts the steps involved in EOA.

A pool of 4 capable candidates, involving another particle with a concentration corresponding to the arithmetical mean of 4 particles, should be found for establishing the global optima (equilibrium state). The pool vector is made using this particle as indicated in Eq (9).

$$\vec{C}_{eq.pool} = \{\vec{C}_{eq(1)}, \vec{C}_{eq(2)}, \vec{C}_{eq(3)}, \vec{C}_{eq(4)}, \vec{C}_{eq(ave)}\} \tag{9}$$

Figure 2. Steps involved in EOA.

In the first generation, the initial particle adjusts the concentration based on $\vec{C}_{eq(1)}$ during the evolution process; but improvement can occur on $\vec{C}_{eq(ave)}$ in the second generation. Later, all the particles with each potential candidate were adapted the evolution procedure was completed.

The exponential component F in Eq. (7) assists EOA in accomplishing a proper balance between exploration and exploitation. λ must be an arbitrary integer within $[0,1]$ to deal with the turnover rate in real-time CV.

$$\vec{F} = e^{-\vec{\lambda}(Itr - Itr_0)} \tag{10}$$

In Eq (10), Itr represents the number of iterations and is formulated as follows:

$$Itr = \left(1 - \frac{Itr}{\text{Max\_}itr}\right) \times \left(a2 \times \frac{Itr}{\text{Max\_}itr}\right) \tag{11}$$

In Eq (11), $\text{Max\_}itr$ indicates the maximal iteration and a_2 manages the EOA's exploitation capability.

Also, the following statement guarantees convergence while increasing the global and local search abilities of the model:

$$\overrightarrow{Itr_0} = \frac{1}{\vec{\lambda}} \times In\left(-a_1 \times sign(\vec{r} - 0.5) \times \left[1 - e^{-\vec{\lambda} Itr}\right]\right) Itr \tag{12}$$

In Eq (12), a_1 and a_2 are used for adjusting the global and local searching abilities of the EOA. The portion sign $(\vec{r} - 0.5)$ is responsible for the exploration and exploitation strategies. The a_1 and a_2 values in EOA are fixed as 2 and 1, correspondingly. The expression is changed as follows by replacing Eq (12) in Eq (10):

$$\vec{F} = a_1 \times sign(\vec{r} - 0.5) \times \left[e^{-\vec{\lambda} Itr} - 1\right] \tag{13}$$

The rate of generation (G) of EOA is used for improving the exploitation that is utilized as a time function. The G of the multi-functional model's 1st-order exponential decay method is formulated as follows:

$$\vec{G} = \overrightarrow{G_0} \times e^{-\vec{k}(Itr - Itr_0)} \tag{14}$$

In Eq (14), G_0 denotes the initial value and k shows the decay parameter.

Finally, assume $k = \lambda$, the following expression is used for the generation rate:

$$\vec{G} = \overrightarrow{G_0} \times e^{-\vec{\lambda}(Itr - Itr_0)} = \overrightarrow{G_0} \times \overrightarrow{F_0} \tag{15}$$

G_0 is calculated using the following expression:

$$\overrightarrow{G_0} = G\vec{C}P \times \left(\vec{C}_{eq} - \vec{\lambda} \times \vec{C}\right) \tag{16}$$

$$G\vec{C}P = \begin{cases} 0.5 \times r1, & r2 \geq 0 \\ 0, & r2 < 0 \end{cases} \tag{17}$$

where parameters $r1$ and $r2$ are randomly generated values within $[0,1]$ and GCP is used for regulating the generation rate.

Based on the prior formula, the final concentration updating equation can be described as follows:

$$\vec{C} = \vec{C}_{eq} + \left(\vec{C} - \vec{C}_{eq}\right) \times \vec{F} + \frac{\vec{G}}{\vec{\lambda V}} \times \left(1 - \vec{F}\right) \tag{18}$$

There are three terms in updating equation:

- At the first term, the equilibrium concentration is accessible.
- In the second term, the global search is accessible.

The third one is responsible for doing a local search process to obtain accurate solutions.

4. Results and discussion

In this section, the experimental outcome of the EOADL-BIS system was tested utilizing four datasets namely Kvasir-SEG [26], ISIC 2018 [27], DRIVE [28], and CHASE-DB1 [29] dataset. Figure 3 depicts the images of the original and masked region. There are 4 datasets namely ISIC 2018, Kvasir-SEG, DRIVE, and CHASE-DB1, selected for testing in the Results and Discussion section, which signify varied medical imaging states. Kvasir-SEG possibly includes gastrointestinal endoscopy pictures, offering an exclusive task in segmenting structures within the digestive method. ISIC 2018 is concentrated on dermatology, connecting the segmentation of skin lesions vital for melanoma recognition. DRIVE, personalized for retinal image study, demands the exact delineation of retinal vessels. CHASE-DB1, devoted to visual coherence tomography scans, offers challenges in segmenting retina and choroid layers. The presence of these datasets safeguards a complete assessment, evaluating the EOADL-BIS system's flexibility across different medical imaging modalities and segmentation tasks, emphasizing its robustness and effectiveness in varied clinical scenarios.

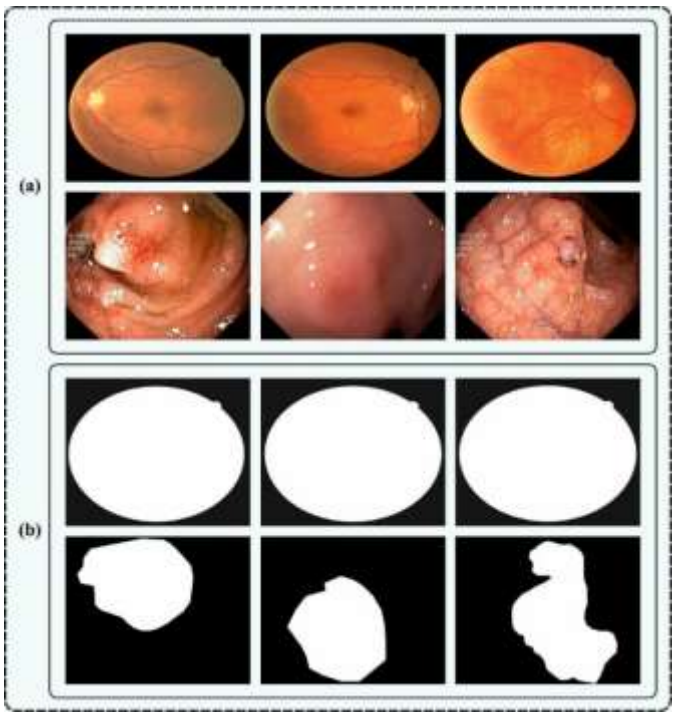

Figure 3. a) Original Images b) Masked Regions.

Table 1 represents the comparative segmentation outcomes of the EOADL-BIS technique on the Kvasir-SEG dataset [13]. Figure 4 represents the $F1_{score}$ and mIoU results of the EOADL-BIS technique with other segmentation approaches on the Kvasir-SEG dataset. The outcomes indicate that the ResUNet++ approach has exposed ineffectual segmentation outcomes with the $F1_{score}$ of 71.43% and mIoU of 61.26%. Moreover, the U-Net++, FCN8, HRNet, DeepLabv3+, and PSPNet models have obtained moderately closer segmentation results. However, the EOADL-BIS system reaches an effectual solution with $F1_{score}$ of 94.28% and mIoU of 94.35%.

Table 1. Comparative outcome of the EOADL-BIS system with recent methods on the Kvasir-SEG database.

Kvasir-SEG Dataset				
Method	**F1-Score**	**mIoU**	**Recall**	**Precision**
U-Net++	80.02	70.00	87.16	79.92
ResUNe ++	71.43	61.26	74.19	78.36
FCN8 Model	83.10	73.65	83.46	88.17
HRNet Model	84.46	75.92	85.88	87.78
PSPNet Model	84.06	74.44	83.57	89.01
DeepLabv3+	86.43	78.62	85.92	90.64
EOADL-BIS	94.28	94.35	93.89	93.91

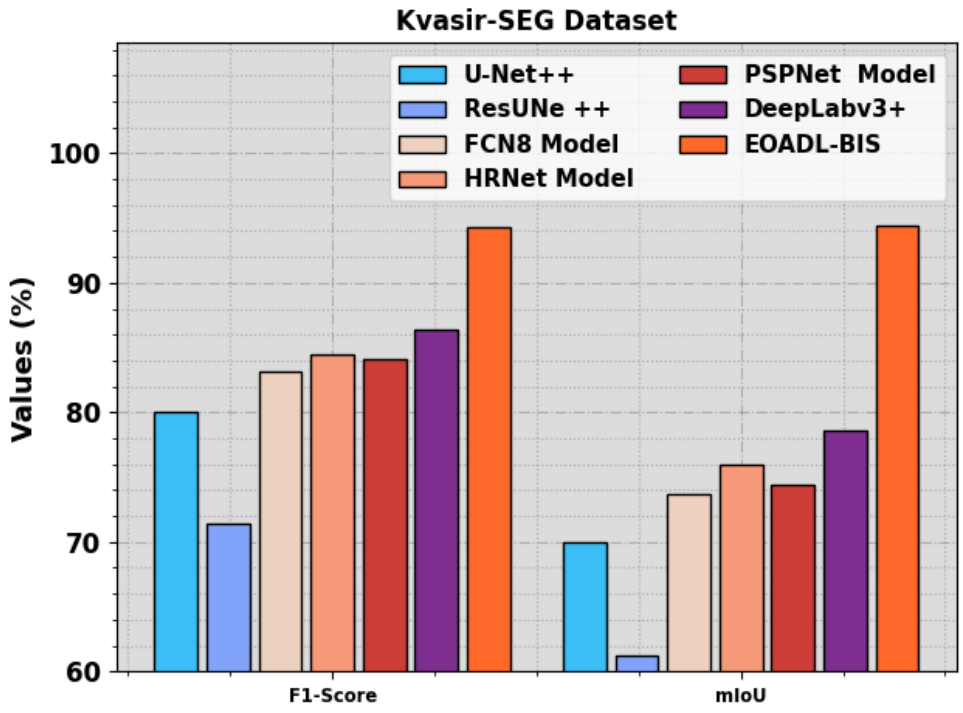

Figure 4. $F1_{score}$ and mIoU outcome of EOADL-BIS algorithm on Kvasir-SEG dataset.

Figure 5 denotes the $reca_l$ and $prec_n$ results of the EOADL-BIS method with other segmentation techniques on the Kvasir-SEG database. The outcomes indicate that the ResUNet++ system has demonstrated ineffectual segmentation outcomes with the $reca_l$ of 74.19% and $prec_n$

of 79.36%. Furthermore, the U-Net++, FCN8, HRNet, DeepLabv3+, and PSPNet techniques have obtained moderately closer segmentation outcomes. However, the EOADL-BIS system achieves efficient performance with a $reca_l$ of 93.89% and $prec_n$ of 93.91%.

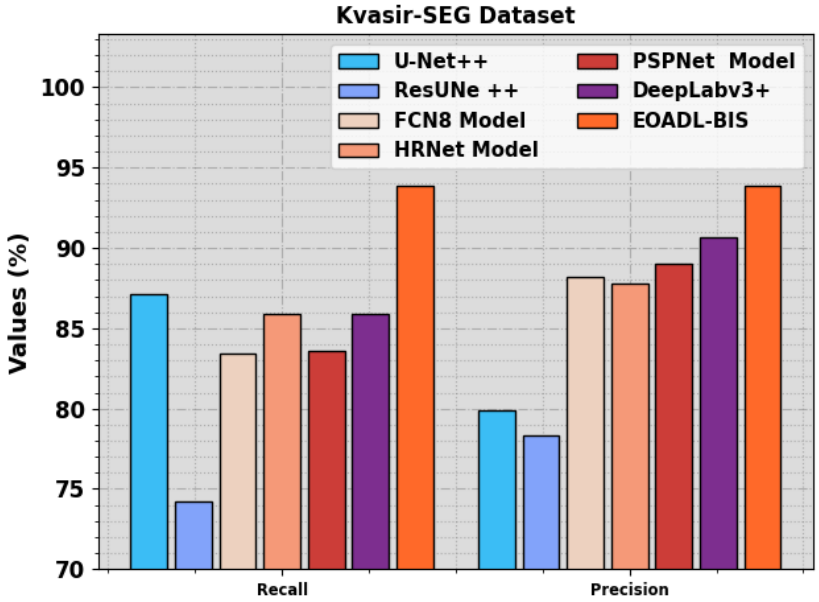

Figure 5. $Reca_l$ and $prec_n$ outcome of EOADL-BIS algorithm on Kvasir-SEG dataset.

Table 2 represents the comparative segmentation analysis of the EOADL-BIS system on the ISIC2018 database. Figure 6 shows the $F1_{score}$, mIoU, and $prec_n$ analysis of the EOADL-BIS approach with other segmentation algorithms on the ISIC2018 datasets. The outcomes indicate that the U-Net system has demonstrated ineffectual segmentation results with a $F1_{score}$ of 67.40%, mIoU of 54.90%, and $prec_n$ of 86.71%. Furthermore, the R2U-Net, Attention R2U-Net, BCDU-Net (d=l), U-Net++, and Attention U-Net methods have obtained moderately closer segmentation results. However, the EOADL-BIS technique achieves effective performance with $a\,F1_{score}$ of 94.11%, mIoU of 94.65%, and $prec_n$ of 94.33%.

Table 2. Comparative outcome of the EOADL-BIS system with recent methodologies on the ISIC2018 database.

ISIC 2018 Dataset					
Method	**F1-Score**	**mIoU**	**Precision**	**Sensitivity**	**Specificity**
U-Net Model	67.40	54.90	86.71	70.80	96.40
R2U-Net Model	67.90	58.10	88.36	79.20	92.80
Attention R2U-Net	69.10	59.20	88.89	72.60	97.00
BCDU-Net (d=l)	84.70	68.03	88.66	78.30	98.00
U-Net++	80.88	73.19	86.48	84.50	91.10
Attention U-Net	82.05	73.46	86.45	85.16	91.35
EOADL-BIS	94.11	94.65	94.33	93.60	98.46

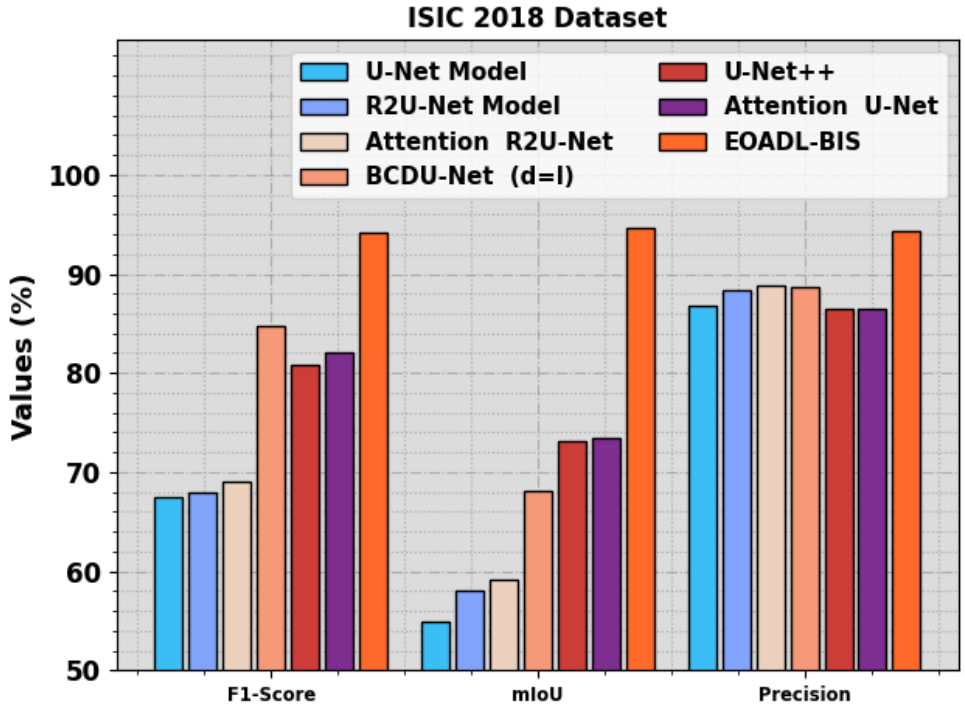

Figure 6. $F1_{score}$, mIoU, and $prec_n$ outcome of EOADL-BIS algorithm on ISIC2018 dataset.

Figure 7 signifies the $sens_y$ and $spec_y$ results of the EOADL-BIS approach with other segmentation techniques on the ISIC2018 dataset. The outcomes indicate that the U-Net system has demonstrated ineffectual segmentation outcomes with a $sens_y$ of 70.80% and $spec_y$ of 96.40%. Additionally, the R2U-Net, Attention R2U-Net, BCDU-Net (d=l), U-Net++, and Attention U-Net systems have acquired moderately closer segmentation results. However, the EOADL-BIS method attains efficient performance with $a\ sens_y$ of 93.60% and $spec_y$ of 98.46%.

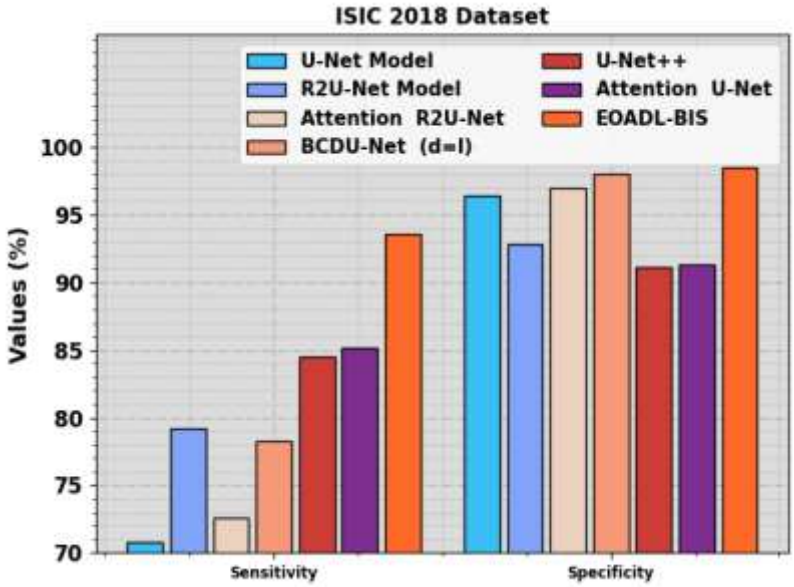

Figure 7. $Sens_y$ and $spec_y$ outcome of EOADL-BIS algorithm on ISIC2018 dataset.

Table 3 represents the comparative segmentation studies of the EOADL-BIS method on the DRIVE database. Figure 8 shows the $F1_{score}$, mIoU, and $prec_n$ analysis of the EOADL-BIS approach with other segmentation algorithms on the DRIVE database. The outcomes indicate that the DenseBlock-UNet model has demonstrated weak segmentation outcomes with the $F1_{score}$ of 81.46%, mIoU of 69.48%, and $prec_n$ of 81.46%. Moreover, the U-Net, Residual U-Net, Recurrent U-Net, R2U-Net, and lterNet systems have achieved moderately closer segmentation outcomes. However, the EOADL-BIS technique reaches efficacious performance with $F1_{score}$ of 95.32%, mIoU of 94.77%, and $prec_n$ of 95.54%.

Table 3. Comparative outcome of EOADL-BIS system with recent methods on DRIVE database.

DRIVE Dataset					
Method	**F1-Score**	**mIoU**	**Precision**	**Sensitivity**	**Specificity**
U-Net Model	81.74	80.42	80.86	78.22	98.08
Residual U Net	81.49	81.16	79.47	76.26	98.20
Recurrent U-Net	81.55	80.00	83.04	75.51	98.16
R2U-Net Model	81.71	84.86	81.83	77.92	98.13
DenseBlock-UNet	81.46	69.48	81.46	79.28	97.76
lterNet Model	82.18	68.98	81.56	77.91	98.31
EOADL-BIS	95.32	94.77	95.54	93.32	98.99

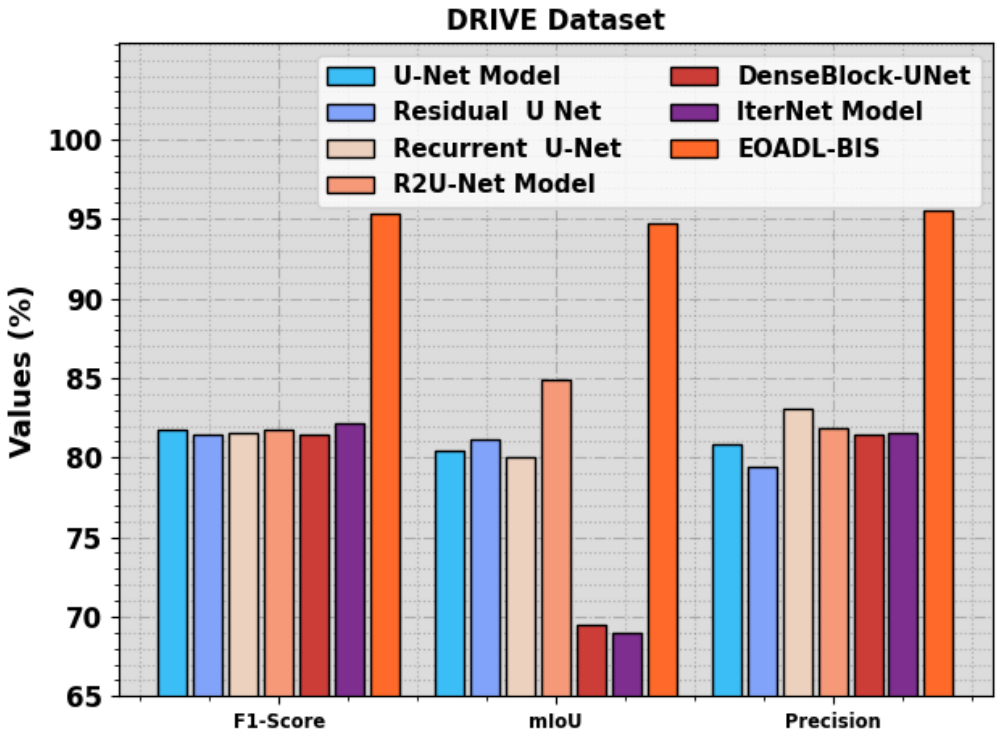

Figure 8. $F1_{score}$, mIoU, and $prec_n$ outcome of EOADL-BIS algorithm on DRIVE dataset.

Figure 9 denotes the $sens_y$ and $spec_y$ results of the EOADL-BIS approach with other segmentation systems on the DRIVE database. The outcomes specify that the DenseBlock-UNet

technique has demonstrated ineffectual segmentation outcomes with a $sens_y$ of 79.28% and $spec_y$ of 97.76%. Furthermore, the U-Net, Residual U-Net, Recurrent U-Net, R2U-Net, and lterNet algorithms have attained moderately closer segmentation outcomes. Nevertheless, the EOADL-BIS methodology gains effectual outcomes with $a\ sens_y$ of 93.32% and $spec_y$ of 98.99%.

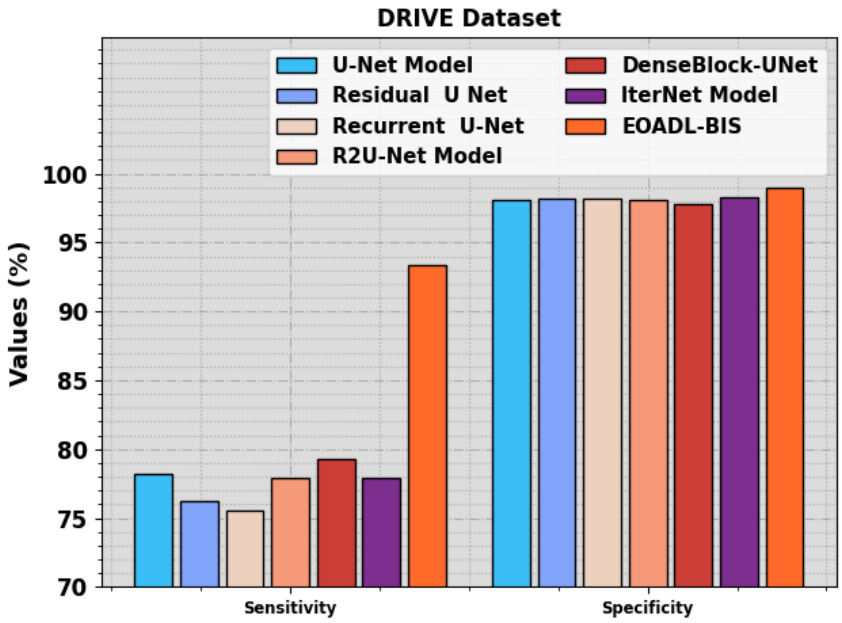

Figure 9. $Sens_y$ and $spec_y$ outcome of EOADL-BIS algorithm on DRIVE dataset.

Table 4 represents the comparative segmentation outcome of the EOADL-BIS technique on the CHASE-DB1 database. Figure 10 denotes the $F1_{score}$, mIoU, and $prec_n$ analysis of the EOADL-BIS approach with other segmentation systems on the CHASE-DB1 database. The outcomes indicated that the Attention U-Net system has demonstrated ineffectual segmentation outcomes with the $F1_{score}$ of 79.41%, mIoU of 69.25%, and $prec_n$ of 78.88%. Additionally, the U-Net, DenseBlock-UNet, IterNet, U-Net++, and FANet algorithms have acquired moderately closer segmentation results. However, the EOADL-BIS approach reaches effectual performance with $F1_{score}$ of 94.94%, mIoU of 94.58%, and $prec_n$ of 94.29%.

Table 4. Comparative outcome of the EOADL-BIS system with recent methodologies on the CHASE-DB1 database.

CHASE-DB1 Dataset					
Method	**F1-Score**	**mIoU**	**Precision**	**Sensitivity**	**Specificity**
U-Net Model	79.93	71.66	79.64	78.40	98.21
DenseBlock-UNet	80.05	70.22	78.81	81.77	96.48
IterNet Model	80.72	72.35	79.96	79.69	97.74
U-Net++	79.54	69.25	78.88	81.14	97.47
Attention U-Net	79.41	65.89	78.52	80.49	98.52
FANet Model	81.08	68.20	77.22	85.44	98.30
EOADL-BIS	94.94	94.58	94.29	94.25	98.97

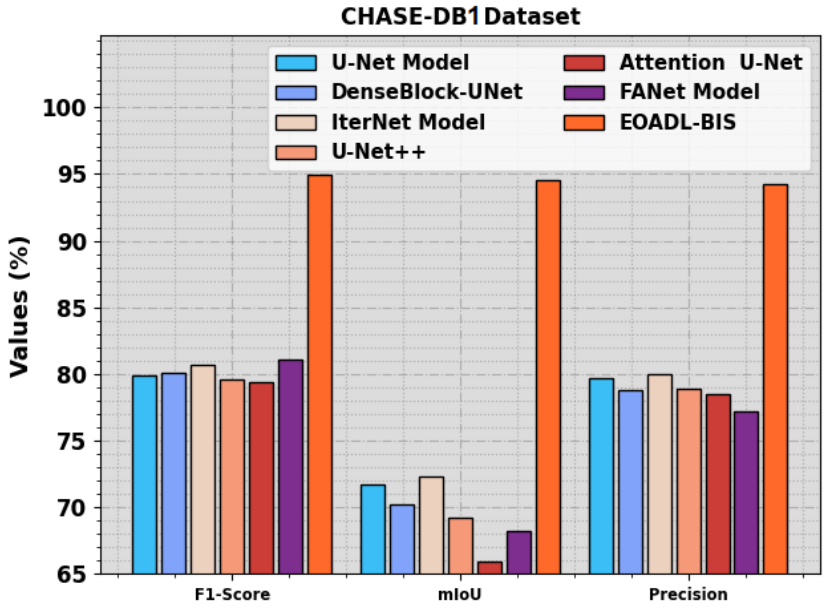

Figure 10. $F1_{score}$, mIoU, and $prec_n$ outcome of EOADL-BIS algorithm on CHASE-DB1dataset.

Figure 11 signifies the $sens_y$ and $spec_y$ results of the EOADL-BIS technique with other segmentation methodologies on the CHASE-DB1 datasets. The outcomes indicated that the Attention U-Net model has demonstrated ineffectual segmentation results with a $sens_y$ of 80.49% and $spec_y$ of 98.52%. Moreover, the U U-Net, DenseBlock-UNet, IterNet, U-Net++, and FANet algorithms have obtained moderately closer segmentation results. However, the EOADL-BIS approach reaches efficacious performance with $a\ sens_y$ of 94.25% and a $spec_y$ of 98.97%.

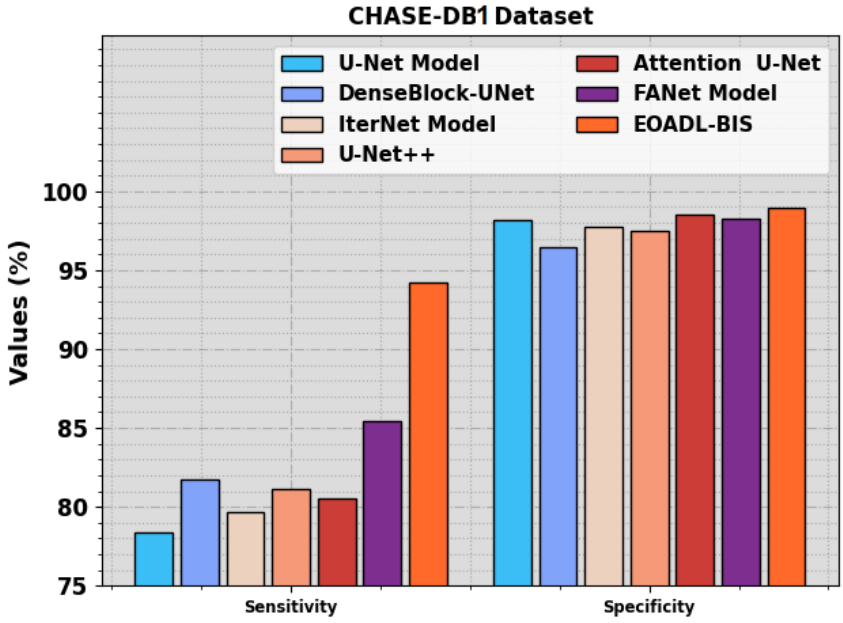

Figure 11. $Sens_y$ and $spec_y$ outcome of EOADL-BIS algorithm on CHASE-DB1dataset.

In Table 5, the EOADL-BIS technique is compared with other DL models concerning distinct measures. The simulation values indicate that the EOADL-BIS algorithm exhibits better performance than other models.

Table 5. Result analysis of the EOADL-BIS algorithm with DL methods.

Method	Params. (million)	Flops (GMac)	Inf. Time (in ms.)	Image size (pixels)
U Net Model	31.04	219.01	3.14	512 × 512
ResU-Net	8.22	181.68	2.93	512 × 512
U-Net++	09.16	138.6	4.07	512 × 512
Attention U-Net	34.88	266.54	4.47	512 × 512
EOADL-BIS	06.92	93.45	9.23	512 × 512

Table 6 and Figure 12 represent the F1-score results of the EOADL-BIS technique on different iterations. The results stated that the EOADL-BIS technique reaches enhanced $F1_{score}$ values under all iterations. For instance, on the Kvasir-SEG dataset, the EOADL-BIS technique offers $a\,F1_{score}$ of 82.44%, 91.60%, 94.05%, 94.18%, and 94.57% under iterations 1–5, respectively. Also, on the DRIVE dataset, the EOADL-BIS algorithm offers a $F1_{score}$ of 80.12%, 82.44%, 82.44, 82.44%, and 82.70% under iterations 1–5, respectively. Finally, on the CHASE-DB1 dataset, the EOADL-BIS approach offers a $F1_{score}$ of 67.35%, 81.67%, 82.18%, 82.06%, and 82.18% under iterations 1–5, correspondingly.

Table 6. $F1_{score}$ analysis of the EOADL-BIS approach with distinct iterations on four datasets.

Iterations	Kvasir-SEG	DRIVE	ISIC 2018	CHASE-DB1
1	82.44	80.12	91.73	67.35
2	91.60	82.44	92.89	81.67
3	94.05	82.44	92.76	82.18
4	94.18	82.44	92.50	82.06
5	94.57	82.70	92.63	82.18

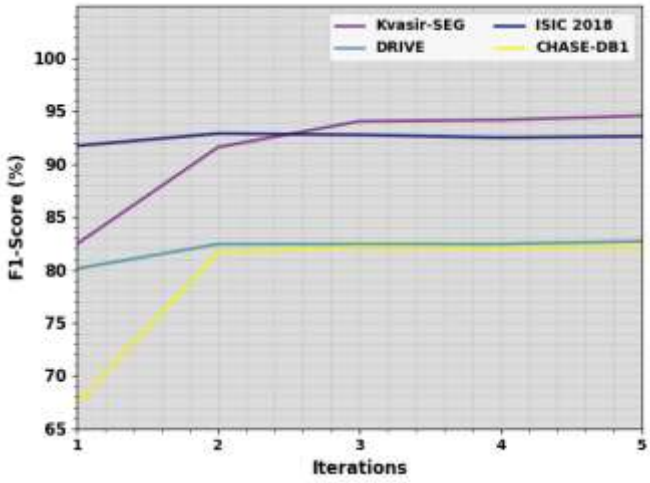

Figure 12. $F1_{score}$ analysis of the EOADL-BIS approach with distinct iterations on four datasets.

These results stated the enhanced outcome of the EOADL-BIS technique over other existing approaches concerning different measures. The superior performance of the EOADL-BIS approach can be recognized by its new combination of the EOA with the Faster RCNN method and ResNeXt design. Unlike customary DL-based biomedical image segmentation techniques, the EOADL-BIS model influences the power of EOA throughout the training procedure of the Faster RCNN method. This unique mixture enhances the hyperparameters of the ResNeXt system, foremost to improve feature removal, enhanced classification accurateness, and exact localization of regions of interest. The use of Faster RCNN with ResNeXt as a backbone system permits effectual region proposal generation over the RPN. This, in turn, enables correct segmentation by leveraging the innovative abilities of ResNeXt for localization and classification. The combination of EOA enhances the model's hyperparameters, safeguarding a modified and well-balanced outline that donates to the complete superior performance of the EOADL-BIS approach. Furthermore, the experimental outcomes across various benchmark datasets, with Kvasir-SEG, ISIC 2018, DRIVE, and CHASE-DB1, reliably establish the efficiency of the EOADL-BIS method. Its strong performance showcases its aptitude to manage diverse medical imaging modalities and segmentation tasks, emphasizing its flexibility and efficacy in contrast to other DL-based segmentation techniques. This new model not only expands accuracy but also finds the tasks of biomedical image segmentation, making the EOADL-BIS model a modern solution in the field**.**

5. Conclusions

In this study, we have concentrated on the development and design of the EOADL-BIS approach for biomedical image segmentation. The main intention of the EOADL-BIS technique is to combine EOA with the Faster RCNN model for an accurate and efficient biomedical image segmentation process. The EOADL-BIS technique comprises two major phases of operations Faster RCNN-based image segmentation and EOA-based hyperparameter tuning. Primarily, the EOADL-BIS technique has employed Faster R-CNN architecture with ResNeXt as a backbone network for image segmentation. Next, the EOA is used to optimize the hyperparameter of the ResNeXt model, which increases the segmentation results and reduces the loss function. The experimental outcome of the EOADL-BIS system was tested on distinct benchmark medical image databases. The simulation results stated the greater outcome of the EOADL-BIS system is related to other DL-based segmentation approaches.

Acknowledgments

The authors extend their appreciation to the Deanship of Scientific Research at King Khalid University for funding this work through a large group Research Project under grant number (RGP2/ 242 /44). Princess Nourah bint Abdulrahman University Researchers Supporting Project number (PNURSP2023R203), Princess Nourah bint Abdulrahman University, Riyadh, Saudi Arabia. Research Supporting Project number (RSPD2024R838), King Saud University, Riyadh, Saudi Arabia. This study is supported via funding from Prince Sattam bin Abdulaziz University project number (PSAU/2023/R/1444). This study is partially funded by the Future University in Egypt (FUE)**.**

Conflict of interest

The authors declare no conflicts of interest.

Use of AI tools declaration

The authors declare that they have not used Artificial Intelligence (AI) tools in the creation of this article.

References

1. S. Chakraborty, K. Mali, An overview of biomedical image analysis from the deep learning perspective, *Research Anthology on Improving Medical Imaging Techniques for Analysis and Intervention*, 2023, 43–59. https://doi.org/10.4018/978-1-6684-7544-7.ch003
2. N. S. Punn, S. Agarwal, Modality specific U-Net variants for biomedical image segmentation: a survey, *Artif. Intell. Rev.*, **55** (2022), 5845–5889. https://doi.org/10.4018/978-1-6684-7544-7.ch003
3. M. Yeung, L. Rundo, Y. Nan, E. Sala, C.B. Schönlieb, G. Yang, Calibrating the Dice loss to handle neural network overconfidence for biomedical image segmentation, *J. Digit. Imaging*, **36** (2023), 739–752. https://doi.org/10.1007/s10278-022-00735-3
4. A. Lou, S. Guan, M. Loew, Cfpnet-m: A lightweight encoder-decoder-based network for multimodal biomedical image real-time segmentation, *Comput. Biol. Med.*, **154** (2023), 106579. https://doi.org/10.1016/j.compbiomed.2023.106579
5. K. A. Davamani, C. R. Robin, S. Amudha, L. J. Anbarasi, Biomedical image segmentation by deep learning methods, *Computational Analysis and Deep Learning for Medical Care: Principles, Methods, and Applications,* 2021, 131–154. https://doi.org/10.1002/9781119785750.ch6
6. A. Shrivastava, M. Chakkaravathy, M. A. Shah, A Comprehensive Analysis of Machine Learning Techniques in Biomedical Image Processing Using Convolutional Neural Networks, In: *2022 5th International Conference on Contemporary Computing and Informatics (IC3I)*, 2022, 1363–1369. IEEE. https://doi.org/10.1109/IC3I56241.2022.10072911
7. A. Iqbal, M. Sharif, M. A. Khan, W. Nisar, M. Alhaisoni, FF-UNet: A U-shaped deep convolutional neural network for multimodal biomedical image segmentation, *Cogn. Comput.*, **14** (2022.), 1287–1302. https://doi.org/10.1007/s12559-022-10038-y
8. N. S. Punn, S. Agarwal, BT-Unet: A self-supervised learning framework for biomedical image segmentation using barlow twins with U-net models. Machine Learning, **111** (2022), 4585–4600. https://doi.org/10.1007/s10994-022-06219-3
9. A. J. Larrazabal, C. Martínez, J. Dolz, E. Ferrante, Orthogonal ensemble networks for biomedical image segmentation, In: *Medical Image Computing and Computer Assisted Intervention–MICCAI 2021: 24th International Conference*, Strasbourg, France, September 27–October 1, 2021, Proceedings, Part III 24, 594–603. Springer International Publishing. https://doi.org/10.1007/978-3-030-87199-4_56

10. Q. Liu, H. Jiang, T. Liu, Z. Liu, S. Li, W. Wen, Y. Shi, Defending deep learning-based biomedical image segmentation from adversarial attacks: A low-cost frequency refinement approach. In: Medical Image Computing and Computer Assisted Intervention–MICCAI 2020: 23rd International Conference, Lima, Peru, October 4–8, 2020, Proceedings, Part IV 23, 342–351. Springer International Publishing. https://doi.org/10.1007/978-3-030-59719-1_34
11. J. Zhang, Y. Zhang, Y. Jin, J. Xu, X. Xu, MDU-Net: multi-scale densely connected U-Net for biomedical image segmentation, Health Information Science and Systems, **11** (2023), 13. https://doi.org/10.1007/978-3-030-59719-1_34
12. S. Pan, X. Liu, N. Xie, Y. Chong, EG-TransUNet: A transformer-based U-Net with enhanced and guided models for biomedical image segmentation, *BMC Bioinformatics*, **24** (2023), 85. https://doi.org/10.1007/978-3-030-59719-1_34
13. N. K. Tomar, D. Jha, M. A. Riegler, H. D. Johansen, D. Johansen, J. Rittscher, et al., Fanet: A feedback attention network for improved biomedical image segmentation, *IEEE Transactions on Neural Networks and Learning Systems*, 2022. https://doi.org/10.1109/TNNLS.2022.3159394
14. M. B. Shuvo, R. Ahommed, S. Reza, M. M. A. Hashem, CNL-UNet: A novel lightweight deep learning architecture for multimodal biomedical image segmentation with false output suppression, *Biomed. Signal Proces.*, **70** (2021), 102959. https://doi.org/10.1016/j.bspc.2021.102959
15. A. Srivastava, D. Jha, S. Chanda, U. Pal, H. D. Johansen, D. Johansen, et al., MSRF-Net: a multi-scale residual fusion network for biomedical image segmentation, *IEEE J. Biomed. Health*, **26** (2021), 2252–2263. https://doi.org/10.1109/JBHI.2021.3138024
16. Z. Zhao, Z. Zeng, K. Xu, C. Chen, C. Guan, Dsal: Deeply supervised active learning from strong and weak labelers for biomedical image segmentation, *IEEE J. Biomed. Health*, **25** (2021), 3744–3751. https://doi.org/10.1109/JBHI.2021.3052320
17. Y. Meng, M. Wei, D. Gao, Y. Zhao, X. Yang, X. Huang, et al., CNN-GCN aggregation enabled boundary regression for biomedical image segmentation, In: Medical Image Computing and Computer Assisted Intervention–MICCAI 2020: 23rd International Conference, Lima, Peru, October 4–8, 2020, Proceedings, Part IV 23, 352–362. Springer International Publishing. https://doi.org/10.1109/JBHI.2021.3052320
18. N. Ibtehaz, M. S. Rahman, MultiResUNet: Rethinking the U-Net architecture for multimodal biomedical image segmentation, *Neural networks*, **121** (2020), 74–87. https://doi.org/10.1109/JBHI.2021.3052320
19. T. Ma, A. V. Dalca, M. R. Sabuncu, Hyper-convolution networks for biomedical image segmentation, In: Proceedings of the IEEE/CVF Winter Conference on Applications of Computer Vision, 2022, 1933–1942.
20. H. Song, Y. Wang, S. Zeng, X. Guo, Z. Li, OAU-net: Outlined Attention U-net for biomedical image segmentation, *Biomed. Signal Proces. Control,* **79** (2023), 104038. https://doi.org/10.1109/JBHI.2021.3052320
21. M. P. Schilling, T. Scherr, F. R. Münke, O. Neumann, M. Schutera, R. Mikut, et al., Automated annotator variability inspection for biomedical image segmentation, *IEEE Access*, **10 (**2022), 2753–2765. https://doi.org/10.1109/ACCESS.2022.3140378
22. R. F. Mansour, N. M. Alfar, S. Abdel-Khalek, M. Abdelhaq, R. A. Saeed, R. Alsaqour, Optimal deep learning based fusion model for biomedical image classification, *Expert Syst.*, **39** (2022), e12764. https://doi.org/10.1111/exsy.12764

23. F. Xie, G. Li, W. Hu, Q. Fan, S. Zhou, Intelligent Fault Diagnosis of Variable-Condition Motors Using a Dual-Mode Fusion Attention Residual, *J. Mar. Sci. Eng.*, **11** (2023), 1385. https://doi.org/10.1111/exsy.12764
24. W. Tang, D. Zou, S. Yang, J. Shi, J. Dan, G. Song, A two-stage approach for automatic liver segmentation with Faster R-CNN and DeepLab, *Neural Comput. Appl.*, **32 (**2020), 6769–6778. https://doi.org/10.1007/s00521-019-04700-0
25. S. N. Makhadmeh, M. A. Al-Betar, K. Assaleh, S. Kassaymeh, A Hybrid White Shark Equilibrium Optimizer for Power Scheduling Problem Based IoT, *IEEE Access*, **10** (2022), 132212–132231. https://doi.org/10.1007/s00521-019-04700-0
26. https://datasets.simula.no/kvasir-seg/
27. https://challenge.isic-archive.com/data/#2018
28. https://drive.grand-challenge.org/
29. https://blogs.kingston.ac.uk/retinal/chasedb1/

AIMS Press